3

10

11

12

13

14

15

16

17

18

19

20

21

22

23

25

26

27

30

Nonlinear evolution of the whistler heat flux instability

ILYA V. KUZICHEV, 1,2 IVAN Y. VASKO, 3,2 ANGEL RUALDO SOTO-CHAVEZ, 1 YUGUANG TONG, 3,4 ANTON V. ARTEMYEV, 5,2 STUART D. BALE, 4,3 AND ANATOLY SPITKOVSKY 6 ¹New Jersey Institute of Technology, Newark, USA

> ²Space Research Institute of Russian Academy of Sciences, Moscow, Russia ³Space Sciences Laboratory, University of California, Berkeley, CA 94720-7450, USA ⁴Physics Department, University of California, Berkeley, CA 94720-7300, USA ⁵ Institute of Geophysics and Planetary Physics, University of California, Los Angeles, USA ⁶Department of Astrophysical Sciences, Princeton University, New Jersey, USA

Submitted to The Astrophysical Journal

ABSTRACT

We use the one-dimensional TRISTAN-MP particle-in-cell code to model the nonlinear evolution of the whistler heat flux instability that was proposed by Gary et al. (1999) and Gary & Li (2000) to regulate the electron heat flux in the solar wind and astrophysical plasmas. The simulations are initialized with electron velocity distribution functions typical for the solar wind. We perform a set of simulations at various initial values of the electron heat flux and β_e . The simulations show that parallel whistler waves produced by the whistler heat flux instability saturate at amplitudes consistent with the spacecraft measurements. The simulations also reproduce the correlations of the saturated whistler wave amplitude with the electron heat flux and β_e revealed in the spacecraft measurements. The major result is that parallel whistler waves produced by the whistler heat flux instability do not significantly suppress the electron heat flux. The presented simulations indicate that coherent parallel whistler waves observed in the solar wind are unlikely to regulate the heat flux of solar wind electrons.

Keywords: solar wind — heat flux — whistler waves

1. INTRODUCTION

The electron heat flux in collisionless or weakly collisional plasma is generally not described by the collisional Spitzer-Härm law (Spitzer & Härm 1953). The heat flux suppression below the collisional value was demonstrated by direct in-situ measurements in the solar wind (Feldman et al. 1975; Scime et al. 1994; Crooker et al. 2003; Bale et al. 2013) and remote observations of the 31 temperature distribution of a hot gas in galaxy clusters (Cowie & McKee 1977; Bertschinger & Meiksin 1986; Fabian 1994; Zakamska & Narayan 2003; Wagh et al. 2014; Fang et al. 2018). The Spitzer-Härm law was hypothesized to be inadequate for describing the heat conduction in the solar corona (Scudder 1992; Landi & Pantellini 2001; Dorelli & Scudder 2003) and that was

Corresponding author: Ilva Kuzichev ilva.kuzichev@njit.edu

recently confirmed in the analysis of coronal loop oscillations (Wang et al. 2015). The observations in the solar wind were interpreted in terms of the heat flux regulation by wave-particle interactions (Feldman et al. 1975, 43 1976; Gary & Feldman 1977; Scime et al. 1994; Crooker et al. 2003), but the wave activity potentially regulating the electron heat flux is still under debate (e.g., Gary et al. 1999; Scime et al. 2001; Pagel et al. 2007; Roberg-Clark et al. 2016; Tong et al. 2018; Roberg-Clark et al. 2018b,a; Komarov et al. 2018; Vasko et al. 2019; Verscharen et al. 2019). The alternative view is that waveparticle interactions may be not necessary to explain the observed heat flux values in the solar wind (Landi et al. 2012, 2014; Horaites et al. 2015).

The mechanism of the electron heat flux regulation is intimately related to kinetic features of the electron velocity distribution function (VDF). The electron VDF in a slow solar wind is often adequately described by a combination of bi-Maxwellian thermal dense core and suprathermal tenuous halo populations (Feldman et al.

1975, 1976; Maksimovic et al. 1997; Tong et al. 2019b). In the plasma rest frame, the core and halo populations are streaming along the background magnetic field, the net electron current is approximately zero, while the electron heat flux is anti-sunward and carried predominantly by halo electrons (Feldman et al. 1975, 1976; Scime et al. 1994; Tong et al. 2019b). In what follows, we focus on a slow solar wind and do not consider effects of the strahl population (anti-sunward beam-like population) frequently observed in a fast solar wind and carrying a significant portion of the electron heat flux (e.g., Rosenbauer et al. 1977; Pilipp et al. 1987; Štverák et al. 2009). 71

73

92

102

At sufficiently large heat flux values electrons are capable of generating whistler waves propagating quasiparallel to the background magnetic field (Gary et al. 1975, 1994). Spacecraft measurements of the electron heat flux values below a bound dependent on β_e (electron beta parameter) were interpreted in terms of the heat flux regulation by this so-called whistler heat flux instability (WHFI) (Feldman et al. 1976; Gary & Feldman 1977; Gary et al. 1999). The argument behind that hypothesis was that the heat flux bound dependent on β_e is similar to the marginal stability threshold of the WHFI. Gary & Li (2000) extrapolated the hypothesis and proposed that the WHFI may regulate the electron heat flux in high- β_e astrophysical plasma. Pistinner & Eichler (1998) called into question that hypothesis, but no detailed analysis of the nonlinear stage of the classical WHFI was performed to support their arguments. Scime et al. (2001) questioned that the WHFI regulates the electron heat flux in the solar wind based on Ulysses measurements.

The simultaneous wave and particle measurements have recently shown that, though intermittently, whistler waves are indeed present in the solar wind and they are predominantly quasi-parallel that is consistent with the WHFI scenario (Lacombe et al. 2014; Stansby et al. 2016; Kajdič et al. 2016; Tong et al. 2019b,a). Tong et al. (2019b) have demonstrated for several events that the whistler waves were indeed generated locally by the WHFI. The extensive statistical analysis by Tong et al. (2019a) has shown that in the solar wind whistler waves have amplitudes typically less than a few hundredths of the background magnetic field. The amplitude is positively correlated with β_e and generally with the electron heat flux. Though the WHFI is indeed operating in the solar wind, there has been no analysis that would establish whistler wave properties in the nonlinear stage of the WHFI and clarify whistler wave effects on the electron heat flux evolution.

In this paper, we present Particle-In-Cell (PIC) simulations of the WHFI using the fully relativistic massively parallelized TRISTAN-MP code (Spitkovsky 2008; Park et al. 2015). The simulations are restricted to parallel whistler waves, because they have the largest growth rates according to the linear theory of the WHFI (Gary et al. 1975, 1994), and initialized with proton and electron VDFs typical for the solar wind. The simulations demonstrate that in a uniform plasma parallel whistler waves produced by the WHFI are incapable of regulating the electron heat flux. The whistler waves are shown to saturate at amplitudes consistent with the recent spacecraft measurements. The paper is organized as follows. We summarize the results of the WHFI linear theory in Section 2, then present results of the PIC simulations in Section 3, discuss and summarize our conclusions in Sections 4 and 5.

2. WHFI LINEAR THEORY

128

In the linear theory of the original WHFI (Gary et al. 1975), the electron VDF consists of Maxwellian core and 130 halo populations streaming along the background mag-131 netic field, $f_e(v_{||}, v_{\perp}) = f_c(v_{||}, v_{\perp}) + f_h(v_{||}, v_{\perp})$, where

$$f_{\alpha} = n_{\alpha} \left(\frac{m_e}{2\pi T_{\alpha}}\right)^{3/2} \exp\left[-\frac{m_e \left(v_{||} - u_{\alpha}\right)^2 + m_e v_{\perp}^2}{2T_{\alpha}}\right],$$

 $_{\mbox{\scriptsize 132}}$ and $n_{\alpha},~u_{\alpha}$ and T_{α} denote density, bulk velocity and temperature of the core $(\alpha = c)$ and halo $(\alpha = h)$ populations, m_e is the electron mass. The electron cur-135 rent in the plasma rest frame is assumed to be zero, $n_c u_c + n_h u_h = 0$. The electron heat flux associated with the core plus halo electron VDF, $q_e = -0.5 n_c u_c (5T_h +$ $m_e u_h^2 - 5T_c - m_e u_c^2$, is often normalized to the freestreaming heat flux value $q_0 = 1.5 n_e T_e (2T_e/m_e)^{1/2}$, where $n_e = n_c + n_h$ is the total electron density, $T_e = (n_c T_c + n_h T_h)/n_e$ is typical macroscopic electron temperature (e.g., Gary et al. 1999). The normalized electron heat flux q_e/q_0 depends on n_c/n_e , T_h/T_c and $u_c\sqrt{m_e/T_c}$. At realistic parameters in the solar wind, thermal protons do not interact resonantly with whistler waves unstable to the WHFI (e.g., Gary et al. 1994; Gary & Li 2000), therefore the contribution of protons to the whistler wave linear dispersion relation is considered in the frame of the cold fluid approach.

At $\omega_{pe} \gg \Omega_e$ the frequency and the linear growth rate of a parallel whistler wave are determined by the 152 following dispersion relation (e.g., Mikhailovskii 1974)

$$\frac{k^2c^2+\omega_{pi}^2}{\omega^2}\approx\frac{\omega_{pe}^2}{\omega^2}\sum_{\alpha=e,b}\frac{n_\alpha}{n_e}\;\frac{(\omega-ku_\alpha)}{kv_\alpha}\;Z\left(\frac{\omega-ku_\alpha-\Omega_e}{kv_\alpha}\right)$$

where ω and k are the whistler wave frequency and wavenumber, ω_{pe} and ω_{pi} are electron and proton

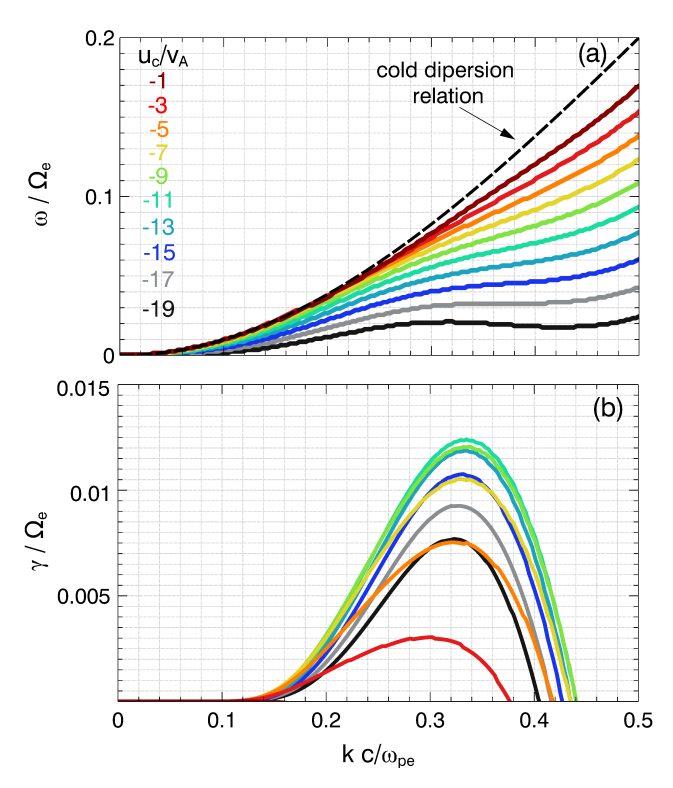


Figure 1. Summary of the linear stability analysis of the whistler heat flux instability in a plasma with $n_c/n_e = 0.85$, $T_h/T_c = 10$ and $\beta_c = 1$. Panels (a) and (b) show dispersion curves and linear growth rates of parallel whistler waves computed at various u_c/v_A , where u_c is the bulk velocity of the core population, $v_A = B_0/(4\pi n_e m_p)^{1/2}$ is the Alfvén velocity. The whistler wave frequency and growth rate are normalized to the electron cyclotron frequency Ω_e , while the wavenumber is normalized to the electron inertial length c/ω_{pe} . Panels (a) and (b) show that the fastest growing whistler waves have wavelengths of about 20 c/ω_{pe} and frequencies below $0.1 \Omega_e$.

plasma frequencies, Ω_e is the electron cyclotron frequency, $Z(\xi) = (2\pi)^{-1/2} \int_{-\infty}^{+\infty} dx \ e^{-x^2/2}/(x-\xi)$ is the plasma dispersion function, $v_{\alpha} = (T_{\alpha}/m_e)^{1/2}$ denotes thermal velocity of the core and halo populations. We solve the dispersion relation in the limit of a weak instability via the standard techniques (e.g., Mikhailovskii 1974). The linear growth rate γ normalized to Ω_e depends on kc/ω_{pe} , n_c/n_e , T_h/T_c , $\beta_c = 8\pi n_c T_c/B_0^2$ and u_c/v_A , where $v_A = B_0/(4\pi n_e m_p)^{1/2}$ is the Alfvén velocity, B_0 is the background magnetic field, m_p is the proton mass. In what follows, we present results of the linear stability analysis of the WHFI for $n_c/n_e = 0.85$ and $T_h = 10 T_c$ if not stated otherwise.

159

160

162

163

164

166

167

170

Figure 1 presents results of the linear stability analysis at $\beta_c=1$ and various u_c/v_A in the range from -1 to -19. Panel (a) shows that the whistler wave dispersion curves are dependent on u_c/v_A and generally different from the whistler dispersion curve in a cold plasma, $\omega=\Omega_e k^2 c^2/(k^2 c^2 + \omega_{pe}^2)$ (e.g., Mikhailovskii 1974). Panel (b) presents the whistler wave growth rates at various u_c/v_A and demonstrates that the growth rates reach maximum values of about $0.01~\Omega_e$ at $kc/\omega_{pe}\approx0.3$. The wavelength of the fastest growing whistler waves is about $20~c/\omega_{pe}$.

We have performed similar growth rate computations at $\beta_c=0.4,2$ and 3 and determined parameters of the fastest growing whistler waves.

Figure 2 presents parameters of the fastest growing whistler waves in dependence on u_c/v_A at various β_c . Panel (a) shows that whistler waves at lower frequencies are preferentially unstable at larger β_c . Panel (b) shows that the growth rate of the fastest growing whistler wave is larger at larger β_c . Panel (c) presents the normalized heat flux q_e/q_0 as a function of u_c/v_A for the further references. The normalized heat flux q_e/q_0 varies with u_c/v_A and β_c , because it depends on $m_e u_c^2/T_c \sim u_c^2/v_A^2\beta_c$. Panels (b) and (c) show that at any given β_c , the growth rate of the fastest growing whistler wave is a non-monotonous function of u_c/v_A or, equivalently, q_e/q_0 (in accordance with Gary 1985).

In addition to the linear theory results for $T_h/T_c=10$, Figure 2 also presents parameters of the fastest growing whistler waves in a plasma with $\beta_c=1$ and $T_h/T_c=1$ 4. The comparison of the growth rates computed at $T_h/T_c=4$ and 10 shows that the smaller halo temperature results in more than five times smaller maximum growth rate. The specific values of u_c/v_A and q_e/q_0

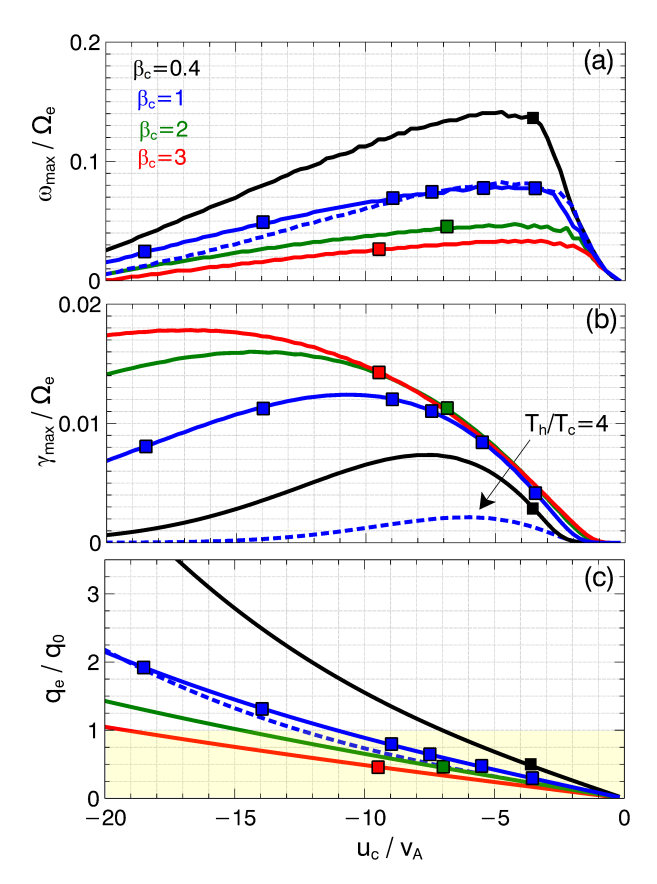


Figure 2. Summary of the linear stability analysis of the whistler heat flux instability in a plasma with $n_c/n_e = 0.85$, $T_h/T_c = 10$ (solid curves) and $n_c/n_e = 0.85$, $T_h/T_c = 4$ (dashed curve). Panels (a) and (b) present frequencies and growth rates of the fastest growing parallel whistler waves at various u_c/v_A and β_c . Panel (c) presents the normalized electron heat flux q_e/q_0 at various u_c/v_A and β_c . The squares correspond to initial conditions for the PIC simulations presented in Section 3. The shaded region in panel (c) indicates that in the realistic solar wind we generally have $q_e/q_0 \lesssim 1$ (e.g., Tong et al. 2019a)

#	$-u_c/v_A$	q_e/q_0
1	3.5	0.3
2	5.5	0.45
3	7.5	0.65
4	9.0	0.8
5	14.0	1.3
6	18.5	1.9

Table 1. Parameters for the first set of simulations performed at $\beta_c = 1$. Indicated are initial values of u_c/v_A and q_e/q_0 . In all these simulations $n_c/n_e = 0.85$, $T_h/T_c = 10$ and $\omega_{pe}/\Omega_e \approx 12.3$. In Figure 2 the initial conditions for the first set of simulations are indicated by the blue squares.

at which the growth rate reaches maximum depend on T_h/T_c and n_c/n_e . For example, panels (b) and (c) show that at $T_h/T_c=10$, the growth rate reaches maximum at $u_c\approx -10\,v_A$ and $q_e/q_0\approx 0.95$, while at $T_h/T_c=4$, it reaches maximum at $u_c\approx -6\,v_A$ and $q_e/q_0\approx 0.5$.

#	β_c	$-u_c/v_A$	ω_{pe}/Ω_{e}
1	0.4	3.5	7.8
2	1	5.5	12.3
3	2	7.8	17.3
4	3	9.5	21.2

Table 2. Parameters for the second set of simulations performed at the same initial heat flux value, $q_e/q_0=0.45$. Indicated are initial values of β_c , u_c/v_A and ω_{pe}/Ω_e . In all simulations $n_c/n_e=0.85$ and $T_h/T_c=10$. In Figure 2 the initial conditions for the second set of simulations are indicated by four squares (red, green, blue and black) at $q_e/q_0=0.45$.

We perform PIC simulations of the WHFI to establish the effect of the whistler waves on the electron heat flux evolution and determine the amplitude of whistler waves in the nonlinear stage. We use the TRISTAN- MP code (Spitkovsky 2008; Park et al. 2015) with both ions and electrons treated as particles at realistic mass ratio. We restrict the analysis to 1D simulations with a single spatial coordinate x along the background mag-

netic field, hence only strictly parallel whistler waves are modelled. The code is initialized with core and halo electron VDFs given by Maxwell-Jüttner distribution functions, which reduce to Maxwell distributions 218 in a non-relativistic limit (that is the case in our simu-219 lations). The initial proton VDF is a Maxwell-Jüttner 220 distribution function with the proton temperature equal to the core electron temperature (that is realistic in the 222 solar wind at 1 AU, see Artemyev et al. 2018). Due 223 to computational limitations, the simulations are performed at ω_{pe}/Ω_e of the order of 10, while in the realistic solar wind this parameter is about ten times larger. 226 At $\beta_c \sim 1$, this implies the temperature of the core population about 100 times larger than in the realistic solar wind (a few keV instead of 10 eV), because $\omega_{pe}/\Omega_e = \beta_c^{1/2} (m_e c^2/2T_c)^{1/2}$. In fact, in all simulations $T_c = 2$ keV, while the specific value of ω_{pe}/Ω_e is determined by β_c . The length of the simulation box 232 is $L_x = 1296 \, c/\omega_{pe}$ that is much larger than the typical wavelength $20 c/\omega_{pe}$ of the fastest growing whistler waves (Figure 1). The temporal and spatial integration steps are $0.09\,\omega_{pe}^{-1}$ and $0.2~c/\omega_{pe}$ that is adequate 236 to reproduce the expected unstable whistler waves. The number of spatial cells is about 6480, the number of 238 particles per cell is $4 \cdot 10^4$, giving the total number of 239 particles $\approx 2.6 \cdot 10^8$. 240

In all simulations, we assume $n_c/n_e = 0.85$ that is realistic for the solar wind (e.g., Maksimovic et al. 2005; Tong et al. 2019b). Typically in the solar wind $T_h/T_c \sim 4$ (e.g., Maksimovic et al. 2005; Tong et al. 2019b), but in all simulations we assume $T_h/T_c = 10$ to have larger initial growth rates and thereby reduce the saturation time of the instability. We perform two set of simulations. In the first set, $\beta_c = 1$ and $\omega_{pe}/\Omega_e \approx 12.3$, while initial values of u_c/v_A and q_e/q_0 are given in Table 1 and indicated in Figure 2. In the second set, the initial electron heat flux is $q_e/q_0 = 0.45$ and simulations are performed at $\beta_c = 0.4 - 3$. The corresponding initial values of u_c/v_A and ω_{pe}/Ω_e are given in Table 2 and indicated in Figure 2. The realistic parameters in the solar wind are $\beta_c \sim 1$, $|u_c|/v_A \lesssim 10$ and $q_e/q_0 \lesssim 1$ (e.g., Tong et al. 2018, 2019b). Several simulations of the first set are performed at u_c/v_A larger than typically observed in the solar wind (Table 1).

241

242

243

245

246

249

250

252

253

254

256

257

259

260

263

Figure 3 presents results of a simulation from the first set with $u_c = -9 v_A$. Panel (a) presents temporal evolution of the magnetic field $B_{\perp}(x,t) = \left(B_z^2 + B_y^2\right)^{1/2}$ perpendicular to the background magnetic field, demonstrating the growth of electromagnetic waves propagating parallel to the electron heat flux. Panel (b) presents the spectrum of the magnetic field B_y around the center of the simulation box, demonstrating that the waves are

at the central frequency of about 0.05 Ω_e and have a bandwidth comparable to the central frequency. Panel (c) presents waveforms of B_y and B_z around the center of the simulation box and shows that the amplitude of the waves is less than 0.1 B_0 . The 90° phase-shift between B_y and B_z , meaning the right-hand polarization, and the wave propagation parallel the electron heat flux prove that the waves are the whistler waves produced by the WHFI. The central frequency of 0.05 Ω_e is consistent with the linear stability theory (Figure 2a). Panel (d) presents the temporal evolution of the whistler wave amplitude averaged over the simulation box, $B_w \equiv \left(L_x^{-1} \int B_{\perp}^2(x,t) dx\right)^{1/2}$. The instability saturates after about 2000 Ω_e^{-1} at the averaged whistler wave amplitudes of $0.03 B_0$. Panel (e) presents the temporal evolution of the growth rate computed as $\gamma = B_w^{-1} dB_w/dt$ and shows that the initial growth rate $\gamma/\Omega_e \sim 0.01$ is consistent with the linear stability theory (Figure 2b).

Figure 4 clarifies the mechanism of the saturation of the WHFI. Panel (a) presents the initial electron VDF, while panel (b) presents the electron VDF after 2000 Ω_e^{-1} that is after the saturation of the instability. Panel (c) presents the difference between electron VDFs at the initial moment and after the saturation of the instability. The scattering by the whistler waves results in redistribution of the phase space density of electrons with $v_{||} \sim -0.3 c$. Namely, electrons with initial parallel velocities $v_{||} \gtrsim -0.3\,c$ are transported to parallel velocities $v_{||} \lesssim -0.3 c$ and vice versa. These are actually electrons in the first normal cyclotron resonance, $v_{\parallel} = v_R \approx (\omega - \Omega_e)/k$ (e.g., Shklyar & Matsumoto 2009; SotoChavez et al. 2014), because at $\omega_{pe}/\Omega_e \approx 9$, $\omega \sim 0.05 \Omega_e$ and $kc/\omega_{pe} \approx 0.3$, we have $v_R \approx (\omega - \Omega_e)/k \approx -0.3 c$. The resonant electrons provide the energy for the whistler wave growth, while the gradual scattering of these electrons by the whistler waves results in saturation of the instability via formation of a "plateau" on the electron VDF (e.g., Kennel & Engelmann 1966; Sagdeev & Galeev 1969; Karpman 1974). Panel (c) shows that the scattering is efficient for electrons with $|v_{\parallel} - v_R| \lesssim \Delta v_R$, where $\Delta v_R \sim 0.2 c$. The finite resonance width Δv_R is due to the finite bandwidth of the whistler waves, $\Delta v_R \approx \Omega_e \Delta k/k^2$, where Δk is the bandwidth of the whistler waves in the wavenumber space. Adopting the cold dispersion relation for estimates, $\omega \approx \Omega_e k^2 c^2/\omega_{pe}^2$, we derive $\Delta v_R \approx$ $|v_R| \Delta \omega / 2\omega \sim 0.2 c$, because the bandwidth $\Delta \omega$ is comparable to the central frequency ω (Figure 3b).

Figure 5 summarizes results of the first set of simulations performed at $\beta_c=1$ and various initial u_c/v_A and q_e/q_0 (Table 1). Panel (a) shows the temporal evolution

6 KUZICHEV ET AL.

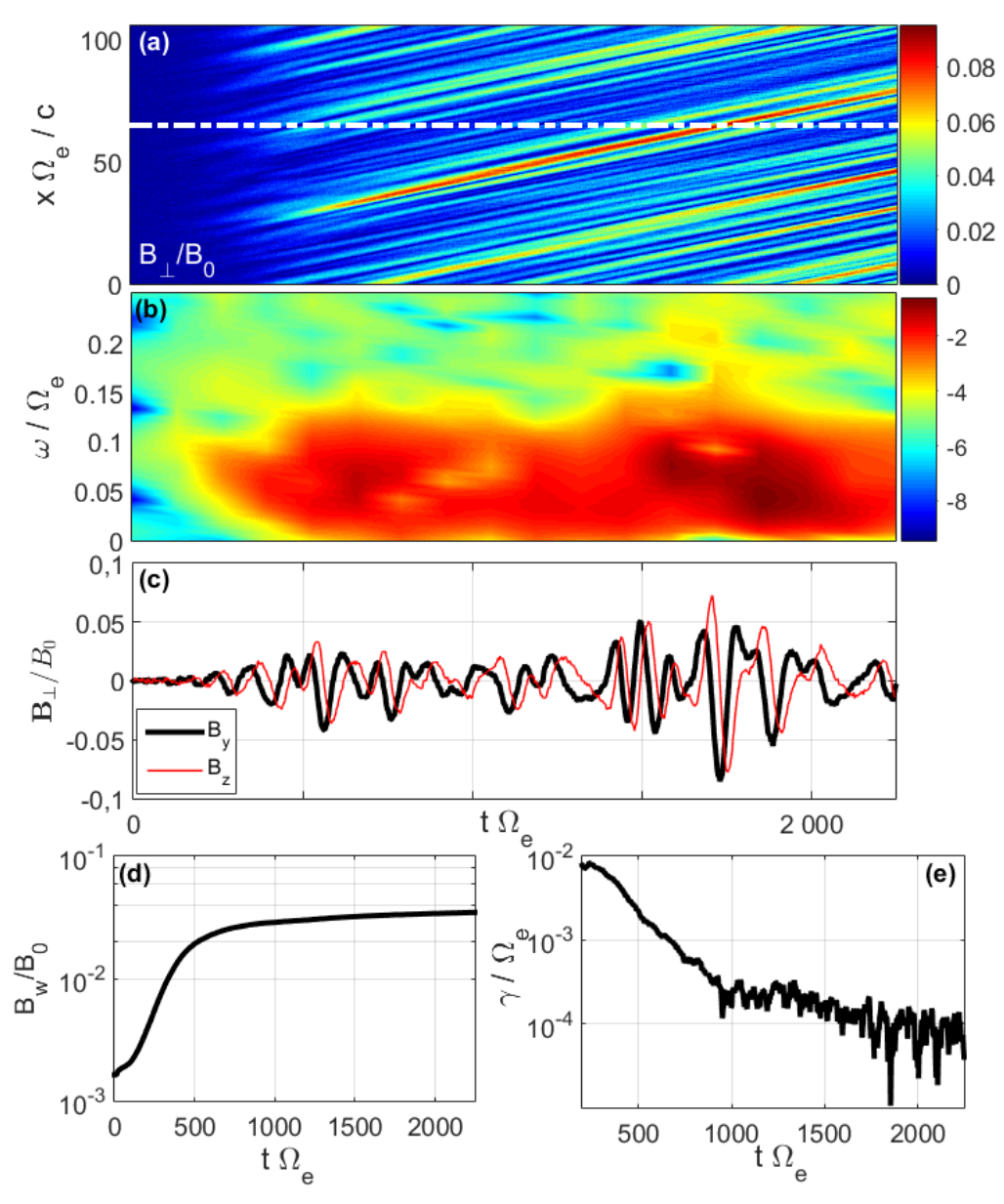


Figure 3. Results of one of the simulations of the first set $(\beta_c = 1$, see Table 1 for other initial parameters) with initial bulk velocity $u_c/v_A = -9$. Panel (a) presents evolution of the whistler wave magnetic field $B_{\perp}(x,t) = (B_y^2 + B_z^2)^{1/2}$, white dashed line marks the position $x_0 = 65 c/\Omega_e$, where we calculate the wave spectrum. Panels (b) presents the spectrum of the magnetic field component $B_y(x_0,t)$, while panel (c) shows temporal evolution of whistler wave magnetic fields $B_y(x_0,t)$ and $B_z(x_0,t)$, demonstrating 90° phase-shift between B_y and B_z . Panels (d,e) present the averaged (over the box) magnetic field amplitude $B_w(t) = \left(L_x^{-1} \int B_\perp^2(x,t) dx\right)^{1/2}$ and the growth rate $\gamma = B_w^{-1} dB_w / dt$.

of the averaged whistler wave amplitudes and demonstrates that the amplitude in the saturation stage depends on the initial heat flux value. The whistler waves 321 saturate at amplitudes of about $0.02 - 0.04 B_0$. Panels (b) and (c) show that the scattering of electrons by the whistler waves result in variations of the electron heat flux and β_c by less than a few percent. The variation of β_c is mostly due to the numerical heating of cold electrons that is recognized by the monotonous growth of

322

323

 β_c . Though the initial heat flux values in the first set of simulations are in the range from 0.3 to 1.9 (Table 1), 330 the heat flux values in the saturation stage differ from the initial values by less than a few percent. These results do not support the scenario that parallel whistler waves produced by the WHFI suppress the electron heat flux below the marginal stability threshold dependent on β_c (Gary et al. 1999; Gary & Li 2000). According 336 to that scenario, the heat flux values in the saturation

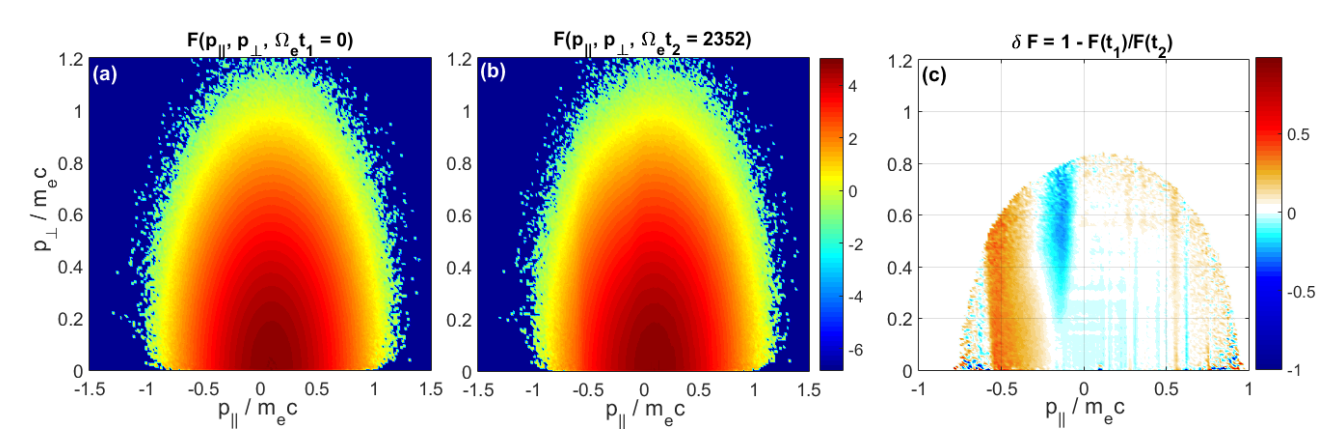


Figure 4. The electron VDFs in the simulation presented in Figure 3. Panels (a) and (b) present electron VDFs at the initial moment and after the saturation of the instability (after 2000 Ω_e^{-1}), respectively. The VDFs are presented in $(p_{||}, p_{\perp})$ plane, where $p_{||,\perp}$ are relativistic electron momenta. Panel (c) shows the difference between the VDFs, $\delta F(p_{||}, p_{\perp}) = 1 - F(p_{||}, p_{\perp}, t_1)/F(p_{||}, p_{\perp}, t_2)$. The phase space density of electrons is redistributed mainly in the region corresponding to the first normal cyclotron resonance, $v_{||} \approx (\omega - \Omega_e)/k$. We masked out $\delta F(p_{||}, p_{\perp})$ at $p_{||}^2 + p_{\perp}^2 \gtrsim m_e^2 c^2$ to avoid effects of statistical noise due to small number of particle in these phase space regions.

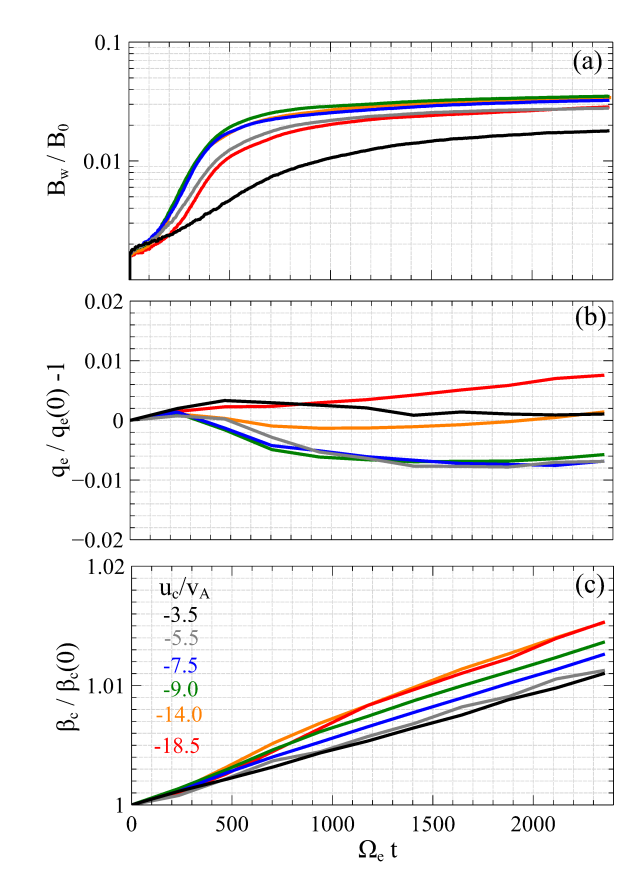


Figure 5. Results of the first set of simulations performed at $\beta_c = 1$ and various u_c/v_A (Table 1). Panel (a) presents temporal evolution of the averaged whistler wave magnetic field amplitude B_w/B_0 , panels (b) and (c) show temporal evolution of the electron heat flux q_e and β_c normalized to their initial values $q_e(0)$ and $\beta_c(0)$. Both q_e and β_c vary by less than a few percent in the course of the instability development and saturation. The monotonous growth of β_c is due to a numerical heating of the core electron population.

stage would decrease down to approximately the same value in all the simulations, because the marginal stability threshold depends only on β_c . Yet, Figure 5 shows that the heat flux does not decrease significantly, remaining almost constant for all the simulations in this set with different initial heat flux values (Table 1).

337

338

340

341

342

344

345

346

347

348

349

351

352

354

355

356

358

359

360

361

362

363

366

367

368

369

370

371

372

373

374

375

376

377

378

387

Figure 6 summarizes results of the second set of simulations performed at the same initial heat flux $q_e/q_0 =$ 0.45 and various β_c (Table 2). Panel (a) presents the temporal evolution of the averaged whistler wave amplitude and demonstrates that the amplitude in the saturation stage depends on β_c . For $\beta_c = 0.4 - 3$, the whistler waves saturate at amplitudes of $0.01 - 0.05 B_0$. We should mention that in the simulation at $\beta_c = 0.4$ the computations were performed up to $3500 \Omega_e^{-1}$, because it takes longer for the instability to saturate at low β_c due to smaller initial growth rates (Figure 2b). Panels (b) and (c) show that the scattering of electrons by the whistler waves results in variation of the heat flux and β_c by less than a few percent. Again, these results do not support the scenario that parallel whistler waves produced by the WHFI suppress the electron heat flux below the marginal stability threshold (Gary et al. 1999; Gary & Li 2000). The heat flux values in the simulations with various β_c differ by less than a few percent, while according to that scenario the heat flux values in the saturation stage would have been different, because the marginal stability threshold depends on β_c .

Figure 7 presents correlations between the whistler wave amplitude in the saturation stage $\max(B_w)/B_0$ and initial parameters of the electron VDF. Panel (a) presents $\max(B_w)/B_0$ found in the first set of simulations versus initial q_e/q_0 and demonstrates that these quantities are positively correlated, though the correlation switches to negative at $q_e/q_0 \gtrsim 0.8$. Panel (b) presents $\max(B_w)/B_0$ found in the second set of simulations versus β_c and demonstrates a positive correlation between these quantities. Panels (a) and (b) also present the linear growth rates $\gamma_{\rm max}/\Omega_e$ of the fastest growing whistler waves corresponding to the performed simulations (Figure 2). There is a clear positive correlation between the whistler wave amplitude in the saturation stage and the initial maximum growth rate. The results of the simulations are well fitted to

$$\max(B_w)/B_0 \sim A \left(\gamma_{\max}/\Omega_e\right)^{\alpha} \tag{1}$$

with $A \sim 0.57$ and $\alpha \sim 0.64$. The specific values of A and α are likely dependent on n_c/n_e and T_h/T_c that were fixed in our simulations, but the positive correlation between $\max(B_w)/B_0$ and γ_{\max}/Ω_e is expected to hold.

4. DISCUSSION

The electron heat flux is one of the leading terms in the electron energy balance in the expanding solar wind (e.g., Cranmer et al. 2009; Stverak et al. 2015), that is why kinetic processes regulating the electron heat flux are of fundamental importance in the solar wind physics. In this paper, we have presented results of 1D PIC simulations demonstrating that in a uniform plasma, the WHFI is incapable of regulating the electron heat flux. In other words, the presented simulations do not support the hypothesis proposed by Gary et al. (1999) and Gary & Li (2000) that whistler waves produced by the WHFI suppress the electron heat flux below the β_e -dependent marginal stability threshold. Though that hypothesis was previously questioned based on theoretical estimates (Pistinner & Eichler 1998) and Ulysses measurements (Scime et al. 2001), no detailed analysis of the nonlinear stage of the WHFI was provided to support those statements. We underline that our conclusions are based on the simulations restricted to parallel whistler waves. Though parallel whistler waves have the largest growth rates (Gary et al. 1975, 1994), 2D PIC simulations should be performed in the future to clarify effects of slightly oblique whistler waves produced by the WHFI.

The recent 1D PIC simulations by Roberg-Clark et al. (2016) have also demonstrated that strictly parallel whistler waves are incapable of regulating the electron heat flux in a collisionless plasma. However, the initial electron VDF set by Roberg-Clark et al. (2016) is an asymptotic solution of the collisional Fokker-Plank equation (e.g., Pistinner & Eichler 1998), that is very different from electron VDFs typical for the solar wind (Feldman et al. 1975; Maksimovic et al. 1997; Tong et al. 2019b). In contrast to Roberg-Clark et al. (2016), we have presented 1D PIC simulations of the classical WHFI with initial electron VDFs more relevant to the solar wind, so that the results of the simulations can be compared to in-situ measurements. We should mention that in the realistic solar wind, the halo population is better fitted to κ -distribution with $\kappa \sim 4$, and typically $T_h/T_c \sim 4$ that is lower than used in our simulations (e.g., Maksimovic et al. 2005; Tong et al. 2019b). Such a choice of distribution function and temperature ratio would affect the quantitative results for linear growth rates, and, consequently, the saturated wave amplitudes (see Equation (1)), as we discuss below. But it does not affect the qualitative results for the WHFI, still producing low-amplitude quasi-parallel whistler waves.

The presented simulations show that whistler waves saturate at amplitudes of about $0.01 - 0.05 B_0$. These amplitudes are comparable to the largest amplitudes of whistler waves measured in the solar wind at 1 AU

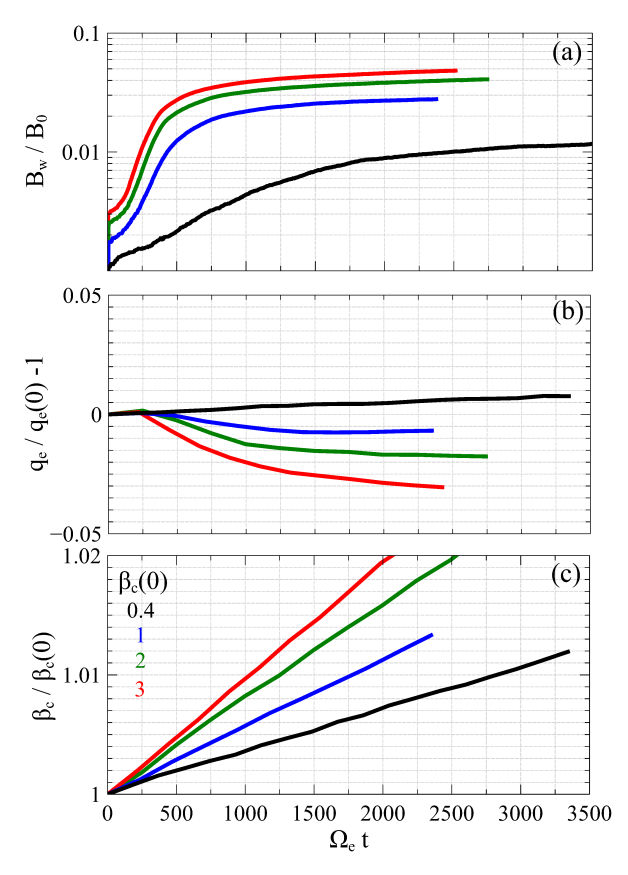


Figure 6. Results of the second set of simulations at various β_c and fixed initial heat flux, $q_e/q_0 = 0.45$ (Table 2). Panel (a) presents temporal evolution of the averaged whistler wave magnetic field amplitude B_w/B_0 , panels (b) and (c) show temporal evolution of the electron heat flux q_e and β_c normalized to their initial values $q_e(0)$ and $\beta_c(0)$. Both q_e and β_c vary by less than a few percent in the course of the instability development and saturation. The monotonous growth of β_c is due to a numerical heating of the core electron population.

(Tong et al. 2019a). Namely, the spacecraft measurements showed that whistler waves amplitudes are generally below $0.02 B_0$, while typical amplitudes are of about 442 $3 \cdot 10^{-3} B_0$ (Tong et al. 2019a). In the simulations with smaller density and temperature of the halo population $(n_c/n_e > 0.85 \text{ and } T_h/T_c < 10)$, whistler waves would certainly saturate at amplitudes smaller than 446 $0.01 - 0.05 B_0$ that would be consistent with the typical amplitudes found in the spacecraft measurements. The simulations have shown that the saturated whistler wave amplitude is positively correlated with β_c that is consis-450 tent with the correlation between the whistler wave amplitude and β_e revealed in the spacecraft measurements 452 (Tong et al. 2019a).

445

448

449

453

455

456

457

Our results demonstrate that the saturated whistler wave amplitude $\max(B_w)/B_0$ depends non-monotonously on q_e/q_0 . It is related to the fact that the initial (linear) maximum growth rate $\gamma_{\rm max}/\Omega_e$ depends on q_e/q_0 non-monotonously (Figure 2), while $\max(B_w)/B_0 \sim$ $A(\gamma_{\rm max}/\Omega_e)^{\alpha}$. Interestingly, similar correlation between the whistler wave amplitude and q_e/q_0 was revealed in

461 the spacecraft measurements, though the correlation switches from positive to negative at $q_e/q_0 \sim 0.3$ (Tong et al. 2019a). Figure 2 shows that at $T_h/T_c \sim 4$ that is more typical in the solar wind (e.g., Maksimovic et al. 2005; Tong et al. 2019b), $\gamma_{\rm max}/\Omega_e$ reaches maximum at $q_e/q_0 \sim 0.5$. Therefore, in simulations with $T_h/T_c = 4$ the correlation between $\max(B_w)/B_0$ and q_e/q_0 would switch from positive to negative at $q_e/q_0 \sim 0.5$ that would be in better agreement with the spacecraft measurements. Tong et al. (2019a) have considered whistler waves in the solar wind not disturbed by shocks, but we note that whistler waves produced by the WHFI were also identified around interplanetary shocks (Wilson et al. 2013; Liu et al. 2018), and a positive correlation between the whistler wave amplitude and electron heat flux was reported (Wilson et al. 2013).

The dependence of the saturated whistler wave amplitude on the initial maximum growth rate is similar to the one established by Tao et al. (2017) in the quasi-linear analysis of the classical temperature-anisotropy instability (Sagdeev & Shafranov 1960; Kennel & Petschek

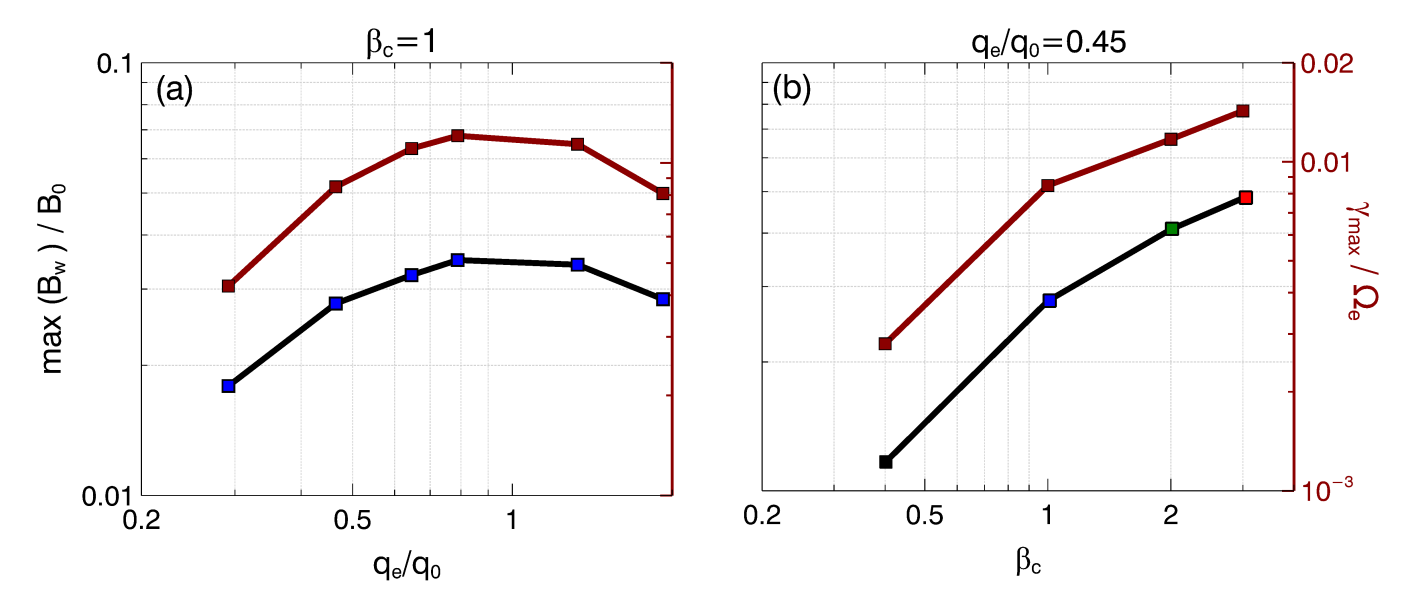


Figure 7. Panel (a) presents the saturated whistler wave amplitude versus initial normalized electron heat flux, as found in the first set of simulations performed at $\beta_c = 1$ and various initial values of u_c/v_A and q_e/q_0 (Table 1). Panel (b) presents the saturated whistler wave amplitude versus initial β_c , as found in the second set of simulations performed at $q_e/q_0 = 0.45$ and various initial values of β_c (Table 2). The saturated whistler wave amplitudes $\max(B_w)/B_0$ are determined after 2000 Ω_e^{-1} for $\beta_c \geq 1$ (see Figure 5) and after 3000 Ω_e^{-1} for $\beta_c = 0.4$ (see Figure 6). In both panels we present the growth rates (brown curve) of the fastest growing whistler wave γ_{\max}/Ω_e derived from the linear stability theory (Figure 2). The squares in panels (a) and (b) are color coded as in Figure 2.

1966). That is not surprising, because the nonlinear evolution of the WHFI seems to be quasi-linear in nature. Whistler waves have rather broad spectrum and saturate at relatively small amplitudes (Figure 3), so that the electron scattering is determined by the finite bandwidth, rather than by the finite amplitude of the whistler waves (Figure 4c). Tong et al. (2019a) have recently demonstrated that the quasi-linear theory is indeed applicable to describe effects of whistler waves observed in the solar wind, thereby demonstrating an adequacy of the previous quasi-linear simulations of whistler wave effects in the solar wind (e.g., Vocks et al. 2005; Vocks 2012).

484

485

486

487

488

489

491

492

493

494

495

496

498

499

500

502

503

505

506

The presented results indicate that there is a fundamental problem concerning processes controlling the electron heat conduction in the solar wind. We have shown that coherent parallel whistler waves observed in the solar wind (Lacombe et al. 2014; Stansby et al. 2016; Kajdič et al. 2016; Tong et al. 2019a,b) are unlikely to regulate the electron heat flux. We underline that we have addressed the evolution of the WHFI in a uniform plasma. Because the saturation time of the WHFI in physical units is from a few seconds to several minutes (see Figures 5a and 6a in this paper and Figure 16 in Tong et al. (2019a)), whistler waves with typical group velocities of thousands km/s may cover a significant spatial region and can be influenced by low-

509 frequency density and magnetic field fluctuations. The analysis of effects of low-frequency fluctuations on the nonlinear evolution of the WHFI deserves a separate study (see, e.g., Breizman & Ruytov 1970; Voshchepynets et al. 2015, for analysis of non-uniform plasma density effects on a beam instability evolution). In addition, the evolution of the WHFI may be influenced by the solar wind expansion, which provides the evolution of the background plasma parameters and may continuously support instability of a particular expanding plasma parcel (e.g., Innocenti et al. 2019, for microscopic effects of the expansion). The effects of a slightly oblique propagation (within 20°, see, e.g., Lacombe et al. 2014: Kajdič et al. 2016) of the observed whistler waves should be addressed in the future, though we note that the slight obliqueness may be also due to uncertainty of measurements. Incoherent whistler waves produced due to a turbulence cascade (see, e.g., Gary et al. 2012) could generally regulate the electron heat flux, but spacecraft measurements indicate that the magnetic field turbulence spectrum is likely dominated by kinetic Alfveń waves (e.g., Bale et al. 2005; Salem et al. 2012; Chen et al. 2013) and the contribution of whistler waves to the turbulence spectrum has not been estimated yet (e.g., Narita et al. 2016; Kellogg et al. 2018). Recent PIC simulations showed that rather oblique and large-amplitude electromagnetic whistler waves (wave normal angle of 566

567

568

569

570

571

572

573

about 45° and saturated amplitude $B_w \sim 0.3B_0$) can be generated in a system with a sustained electron temperature gradient and suppress the electron heat flux (Komarov et al. 2018; Roberg-Clark et al. 2018b,a). The 539 analysis of magnetic field spectra showed no evidence for such oblique whistler waves in the solar wind at 1 AU 541 (e.g., Tong et al. 2019a). The likely reason is that the electron VDF developing in those simulations is very different from what is observed in the solar wind. In particular, Landau resonant electrons damp too oblique whistler waves in the solar wind (that is why the WHFI of electron VDFs typical for the solar wind produces 547 only quasi-parallel whistler waves) (Gary et al. 1994), while Landau resonant electrons seem to drive oblique whistler waves in the simulations by Roberg-Clark et al. 550 (2018a). Thus, it is currently not clear what processes 551 regulate the electron heat flux in the solar wind (see Vasko et al. 2019; Verscharen et al. 2019, for a recent discussion), while simulations presented in this paper exclude coherent parallel whistler waves in a uniform 555 plasma from the list of potential processes.

5. CONCLUSION

557

561

562

563

564

565

We have presented results of 1D PIC simulations of the whistler heat flux instability. We summarize the results as follows:

- 1. In a uniform plasma, parallel whistler waves produced by the whistler heat flux instability are incapable of regulating the electron heat flux.
- 2. Whistler waves saturate at amplitudes consistent with the recent spacecraft measurements. The

simulations reproduce the correlations of the saturated whistler wave amplitude with the electron heat flux q_e/q_0 and β_e revealed in the spacecraft measurements.

3. The saturated whistler wave amplitudes are dependent on the maximum growth rate computed from the linear theory, $\max(B_w)/B_0 \sim A(\gamma_{\max}/\Omega_e)^{\alpha}$.

The presented simulations exclude coherent parallel whistler waves observed in the solar wind from the list of potential processes regulating the electron heat flux. The effects of non-uniform background plasma density and magnetic field and slightly oblique propagation of the observed whistler waves remain to be addressed.

I. Kuzichev and A. R. Soto-Chavez were supported by the National Science Foundation (NSF) grant No. 1502923. They would like to acknowledge high-performance computing support from Cheyenne (doi:10.5065/D6RX99HX) provided by NCAR's Computational and Information Systems Laboratory, sponsored by NSF. The NJIT Kong cluster at New Jersey Institute of Technology (Newark, NJ, USA) was also used. I. Kuzichev would also like to acknowledge the support of the RBSPICE Instrument project by JHU/APL subcontract 937836 to the New Jersey Institute of Technology under NASA Prime contract NAS5-01072. Y. Tong and S. D. Bale were supported in part by NASA contract NNN06AA01C.

REFERENCES

```
Artemyev, A. V., Angelopoulos, V., & McTiernan, J. M.
     2018, Journal of Geophysical Research: Space Physics,
595
     123, 9955, doi: 10.1029/2018JA025904
596
   Bale, S. D., Kellogg, P. J., Mozer, F. S., Horbury, T. S., &
     Reme, H. 2005, Physical Review Letters, 94, 215002,
598
     doi: 10.1103/PhysRevLett.94.215002
599
   Bale, S. D., Pulupa, M., Salem, C., Chen, C. H. K., &
     Quataert, E. 2013, ApJL, 769, L22,
601
     doi: 10.1088/2041-8205/769/2/L22
602
   Bertschinger, E., & Meiksin, A. 1986, ApJL, 306, L1,
     doi: 10.1086/184692
604
   Breizman, B. N., & Ruytov, D. D. 1970, JETP, 30, 759
605
   Chen, C. H. K., Boldyrev, S., Xia, Q., & Perez, J. C. 2013,
606
     Physical Review Letters, 110, 225002,
607
     doi: 10.1103/PhysRevLett.110.225002
608
```

```
Cowie, L. L., & McKee, C. F. 1977, ApJ, 211, 135,
     doi: 10.1086/154911
   Cranmer, S. R., Matthaeus, W. H., Breech, B. A., &
611
     Kasper, J. C. 2009, ApJ, 702, 1604,
612
     doi: 10.1088/0004-637X/702/2/1604
613
   Crooker, N. U., Larson, D. E., Kahler, S. W., Lamassa,
614
     S. M., & Spence, H. E. 2003, Geophys. Res. Lett., 30,
615
     1619, doi: 10.1029/2003GL017036
616
   Dorelli, J. C., & Scudder, J. D. 2003, Journal of
617
     Geophysical Research (Space Physics), 108, 1294,
618
     doi: 10.1029/2002JA009484
619
   Fabian, A. C. 1994, ARA&A, 32, 277,
620
     doi: 10.1146/annurev.aa.32.090194.001425
   Fang, X.-E., Guo, F., Yuan, Y.-F., & Mou, G. 2018, ApJ,
     863, 177, doi: 10.3847/1538-4357/aad1f6
623
```

Liu, M., Liu, Y. D., Yang, Z., Wilson, L. B., I., & Hu, H.

2018, ApJL, 859, L4, doi: 10.3847/2041-8213/aac269

Feldman, W. C., Asbridge, J. R., Bame, S. J., et al. 1976, Maksimovic, M., Pierrard, V., & Riley, P. 1997, 624 Geophys. Res. Lett., 24, 1151, doi: 10.1029/97GL00992 J. Geophys. Res., 81, 5207. 625 doi: 10.1029/JA081i028p05207 Maksimovic, M., Zouganelis, I., Chaufray, J.-Y., et al. 2005, 676 626 Feldman, W. C., Asbridge, J. R., Bame, S. J., Montgomery, Journal of Geophysical Research (Space Physics), 110, 627 M. D., & Gary, S. P. 1975, J. Geophys. Res., 80, 4181, A09104, doi: 10.1029/2005JA011119 678 628 doi: 10.1029/JA080i031p04181 Mikhailovskii, A. B. 1974, Theory of Plasma Instabilities: 629 Gary, S. P. 1985, J. Geophys. Res., 90, 10, Instabilities of a Homogeneous Plasma 680 630 doi: 10.1029/JA090iA11p10815 Narita, Y., Nakamura, R., Baumjohann, W., et al. 2016, 631 Gary, S. P., Chang, O., & Wang, J. 2012, ApJ, 755, 142, ApJL, 827, L8, doi: 10.3847/2041-8205/827/1/L8 632 doi: 10.1088/0004-637X/755/2/142 Pagel, C., Gary, S. P., de Koning, C. A., Skoug, R. M., & 633 Gary, S. P., & Feldman, W. C. 1977, J. Geophys. Res., 82, Steinberg, J. T. 2007, Journal of Geophysical Research 634 1087, doi: 10.1029/JA082i007p01087 (Space Physics), 112, A04103, 635 685 Gary, S. P., Feldman, W. C., Forslund, D. W., & doi: 10.1029/2006JA011967 Montgomery, M. D. 1975, J. Geophys. Res., 80, 4197, Park, J., Caprioli, D., & Spitkovsky, A. 2015, Phys. Rev. doi: 10.1029/JA080i031p04197 Lett., 114, 085003, doi: 10.1103/PhysRevLett.114.085003 638 Gary, S. P., & Li, H. 2000, ApJ, 529, 1131, Pilipp, W. G., Miggenrieder, H., Montgomery, M. D., et al. 639 689 doi: 10.1086/308294 1987, J. Geophys. Res., 92, 1075, 640 Gary, S. P., Scime, E. E., Phillips, J. L., & Feldman, W. C. doi: 10.1029/JA092iA02p01075 641 1994, J. Geophys. Res., 99, 23, doi: 10.1029/94JA02067 Pistinner, S. L., & Eichler, D. 1998, MNRAS, 301, 49, 642 doi: 10.1046/j.1365-8711.1998.01770.x Gary, S. P., Skoug, R. M., & Daughton, W. 1999, Physics 643 693 of Plasmas, 6, 2607, doi: 10.1063/1.873532 Roberg-Clark, G. T., Drake, J. F., Reynolds, C. S., & 694 644 Horaites, K., Boldyrev, S., Krasheninnikov, S. I., et al. Swisdak, M. 2016, ApJL, 830, L9, 645 695 2015, Physical Review Letters, 114, 245003, doi: 10.3847/2041-8205/830/1/L9 646 696 doi: 10.1103/PhysRevLett.114.245003 2018a, Physical Review Letters, 120, 035101, 697 647 Innocenti, M. E., Tenerani, A., & Velli, M. 2019, ApJ, 870, doi: 10.1103/PhysRevLett.120.035101 698 648 66, doi: 10.3847/1538-4357/aaf1be Roberg-Clark, G. T., Drake, J. F., Swisdak, M., & 649 699 Reynolds, C. S. 2018b, ApJ, 867, 154, Kajdič, P., Alexandrova, O., Maksimovic, M., Lacombe, C., 700 650 & Fazakerley, A. N. 2016, ApJ, 833, 172, doi: 10.3847/1538-4357/aae393 701 651 Rosenbauer, H., Schwenn, R., Marsch, E., et al. 1977, 652 doi: 10.3847/1538-4357/833/2/172 Karpman, V. I. 1974, SSRv, 16, 361, Journal of Geophysics Zeitschrift Geophysik, 42, 561 653 doi: 10.1007/BF00171564 Sagdeev, R. Z., & Galeev, A. A. 1969, Nonlinear Plasma Kellogg, P. J., Goetz, K., & Monson, S. J. 2018, ApJ, 853, Theory 655 14, doi: 10.3847/1538-4357/aa93df Sagdeev, R. Z., & Shafranov, V. D. 1960, Soviet JETP, 39, Kennel, C. F., & Engelmann, F. 1966, Physics of Fluids, 9, 657 707 2377, doi: 10.1063/1.1761629 Salem, C. S., Howes, G. G., Sundkvist, D., et al. 2012, 708 Kennel, C. F., & Petschek, H. E. 1966, J. Geophys. Res., ApJL, 745, L9, doi: 10.1088/2041-8205/745/1/L9 709 71, 1, doi: 10.1029/JZ071i001p00001 Scime, E. E., Bame, S. J., Feldman, W. C., et al. 1994, 710 660 Komarov, S., Schekochihin, A. A., Churazov, E., & J. Geophys. Res., 99, 23, doi: 10.1029/94JA02068 661 711 Spitkovsky, A. 2018, Journal of Plasma Physics, 84, Scime, E. E., Littleton, J. E., Gary, S. P., Skoug, R., & Lin, 712 662 905840305, doi: 10.1017/S0022377818000399 N. 2001, Geophys. Res. Lett., 28, 2169, 713 663 Lacombe, C., Alexandrova, O., Matteini, L., et al. 2014, doi: 10.1029/2001GL012925 714 664 ApJ, 796, 5, doi: 10.1088/0004-637X/796/1/5 Scudder, J. D. 1992, ApJ, 398, 319, doi: 10.1086/171859 665 Landi, S., Matteini, L., & Pantellini, F. 2012, ApJ, 760, Shklyar, D., & Matsumoto, H. 2009, Surveys in Geophysics, 666 143, doi: 10.1088/0004-637X/760/2/143 30, 55, doi: 10.1007/s10712-009-9061-7 717 667 —. 2014, ApJL, 790, L12, SotoChavez, A. R., Wang, G., Bhattacharjee, A., Fu, G. Y., 718 668 doi: 10.1088/2041-8205/790/1/L12 & Smith, H. M. 2014, Geophys. Res. Lett., 41, 1838, 719 669 Landi, S., & Pantellini, F. G. E. 2001, A&A, 372, 686, doi: 10.1002/2014GL059320 670 doi: 10.1051/0004-6361:20010552 Spitkovsky, A. 2008, ApJL, 682, L5, doi: 10.1086/590248

Spitzer, L., & Härm, R. 1953, Physical Review, 89, 977,

doi: 10.1103/PhysRev.89.977

723

- Stansby, D., Horbury, T. S., Chen, C. H. K., & Matteini, L.
 2016, ApJL, 829, L16, doi: 10.3847/2041-8205/829/1/L16
 Stverak, S., Traśncek, P. M., & Hellinger, P. 2015, Journal of Geophysical Research: Space Physics, 120, 8177,
- ⁷²⁸ doi: 10.1002/2015JA021368
- ⁷²⁹ Tao, X., Chen, L., Liu, X., Lu, Q., & Wang, S. 2017,
- 730 Geophys. Res. Lett., 44, 8122,
- doi: 10.1002/2017GL074881
- 732 Tong, Y., Bale, S. D., Salem, C., & Pulupa, M. 2018, arXiv
- e-prints. https://arxiv.org/abs/1801.07694
- Tong, Y., Vasko, I. Y., Artemyev, A. V., Bale, S. D., &
- ⁷³⁵ Mozer, F. S. 2019a, ApJ, 878, 41,
- doi: 10.3847/1538-4357/ab1f05
- 737 Tong, Y., Vasko, I. Y., Pulupa, M., et al. 2019b, ApJL, 870,
- T38 L6, doi: 10.3847/2041-8213/aaf734
- ⁷³⁹ Štverák, Š., Maksimovic, M., Trávníček, P. M., et al. 2009,
- Journal of Geophysical Research (Space Physics), 114,
- 741 A05104, doi: 10.1029/2008JA013883
- ⁷⁴² Vasko, I. Y., Krasnoselskikh, V., Tong, Y., et al. 2019,
- ⁷⁴³ ApJL, 871, L29, doi: 10.3847/2041-8213/ab01bd

- Verscharen, D., Chandran, B. D. G., Jeong, S.-Y., et al.
- ⁷⁴⁵ 2019, arXiv e-prints, arXiv:1906.02832.
- 746 https://arxiv.org/abs/1906.02832
- 747 Vocks, C. 2012, SSRv, 172, 303,
 - 8 doi: 10.1007/s11214-011-9749-0
- ⁷⁴⁹ Vocks, C., Salem, C., Lin, R. P., & Mann, G. 2005, ApJ,
- 750 627, 540, doi: 10.1086/430119
- Voshchepynets, A., Krasnoselskikh, V., Artemyev, A., &
- ⁷⁵² Volokitin, A. 2015, ApJ, 807, 38,
- doi: 10.1088/0004-637X/807/1/38
- ⁷⁵⁴ Wagh, B., Sharma, P., & McCourt, M. 2014, MNRAS, 439,
- 755 2822, doi: 10.1093/mnras/stu138
- Vang, T., Ofman, L., Sun, X., Provornikova, E., & Davila,
- J. M. 2015, ApJL, 811, L13,
- doi: 10.1088/2041-8205/811/1/L13
- 759 Wilson, L. B., Koval, A., Szabo, A., et al. 2013, Journal of
- Geophysical Research (Space Physics), 118, 5,
- doi: 10.1029/2012JA018167
- ⁷⁶² Zakamska, N. L., & Narayan, R. 2003, ApJ, 582, 162,
- doi: 10.1086/344641